* Electronic supplementary information

Universal description of heating-induced reshaping preference in core-shell bimetallic nanoparticles

Zheng Zhao[a], Haoxiang Xu[a], Yi Gao[b,c], Daojian Cheng[a*]*

[a]State Key Laboratory of Organic-Inorganic Composites, Beijing Key Laboratory of Energy Environmental Catalysis, Beijing University of Chemical Technology, Beijing100029, China

E-mail: chengdj@mail.buct.edu.cn

[b]Division of Interfacial Water and Key Laboratory of Interfacial Physics and Technology, Shanghai Institute of Applied Physics, Chinese Academy of Sciences, Shanghai 201800, China

[c]Shanghai Advanced Research Institute, Chinese Academy of Sciences, Shanghai, 201210 China

E-mail: gaoyi@sinap.ac.cn

Contents

Supplementary Methods

1. Theoretical model

Based on the effective Ising Hamiltonian model, the definition of Δh_i^{eff}, Δh_i^{size}, and V_{ij} before introducing T can be written as

$$\Delta h_i^{eff} = \chi \Delta\gamma(\alpha) = \chi\left[\gamma_i^B(\alpha) - r_i^A(\alpha)\right] \quad \text{(S1)}$$

$$\Delta h_i^{size} = \Delta E_r = z_i^B \lambda \exp\left[-r^B / \nu\right] - z_i^A \lambda \exp\left[-r^A / \nu\right] \quad \text{(S2)}$$

$$V_{ij} = \frac{1}{2}\left[E_{b(ij)}^{AA} + E_{b(ij)}^{BB} - 2E_{b(ij)}^{AB}\right] \quad \text{(S3)}$$

$$E_{b(ij)} = E_c + E_{pro} + E_{pol} \quad \text{(S4)}$$

where $\gamma(\alpha)$ is the surface energy at different shape factors α. χ is the second moment approximation coefficients.[1] Z_i is the coordination number of an atom at site *i*. *r* is the atom radius. λ and ν are the constants determined by fitting to the bulk modulus and atomic volume.[2] E_c and E_{pol} are the cohesive energy and polarisation energies from literature.[3] E_{pro} is the promotion energy required to take the atom from its ground-state configuration to the magnetic ground-state configuration of the prepared atom, which can be obtained from experimental data[4].

2. The TB-SMA Potential and Monte Carlo (MC) simulation

Monte Carlo (MC) simulation is firstly used to obtain the equilibrium structures of bimetallic nanoparticles as the initial configurations in the following MD simulation. The interaction between metal atoms was modeled semi-empirically based on the well-established TB-SMA potential [5]. It is noted that TB-SMA potential has been successfully used to model the thermodynamic properties of bimetallic nanoparticles effectively.[6-7] In the Gupta potential, the metal-metal (M-M) interaction energy, E_{M-M}, is given by

$$E_{M-M} = \sum_i E_R^i + E_B^i \qquad \text{(S5)}$$

where E_R^i and E_B^i are the Born-Mayer ion-ion repulsion and band interactions, respectively. These two terms for an atom i can be represented based on

$$E_R^i = \sum_{j \neq 1} A e^{-p(r_{ij}/r_0 - 1)} \qquad \text{(S6)}$$

$$E_B^i = -\left\{ \sum_j \xi^2 e - 2q(r_{ij}/r_0 - 1) \right\} \qquad \text{(S7)}$$

where r_{ij} is the distance between atoms i and j in the cluster, r_0 is the nearest-neighbor distance in the pure metals, and N is the number of the metal atoms. The parameters A, r_0, ξ, p, and q for the Ag-Cu, Au-Pd, Ag-Au, and Pd-Cu nanoparticles used in this study are taken from the literature [5, 8] as listed in Table S1, which were employed in previous studies with satisfactory results [9-10] and proved by experiment elsewhere [11-12]. In MC simulations, the integration time step was set to 1 fs and 4 ns are adopted for the total simulation length to achieve the most stable structure. The former 2 ns are performed to make the system equilibrium and the next 2 ns were used for the statistical averaging. When this method is used to study the bimetallic nanoparticles, two trials are introduced in the sampling scheme: (1) random displacement of each atom from its original position and (2) random interchange of two atoms with different species in the cluster.

2. Molecular dynamics simulations

We identify the melting of bimetallic nanoparticles from the caloric curve of the bimetallic nanoparticles and the corresponding heat capacity Cv per atom. According to the position of the maximum peak value in the heat capacity Cv and the step jump

in the caloric curve, and then the melting temperature can be predicted. The heat capacity Cv per atom is defined by

$$Cv = \frac{\left(\langle E^2 \rangle - \langle E \rangle^2\right)}{nk_B T^2} \qquad \text{(S8)}$$

where E is the potential energy, k_B is the Boltzmann constant, n is the total number of the atoms in the cluster and T is the temperature. The transition probability of atoms from state i to state j

$$p_{ij} = \frac{p_i}{p_j} = \exp\left[-(E_i - E_j)/k_B T\right] \qquad \text{(S9)}$$

Where E_i and E_j are the energy for an atom of type A at site i and an atom of type B at site j. In the BOMD simulation, the Perdew−Burke−Ernzerhof (PBE) exchange−correlation functional are used in this work as implemented in the *CP2K* package[13]. The spatial dimension of the simulation super cell is 55 × 55 × 55 Å with a vacuum distance 18 Å, which is large enough to neglect interaction among adjacent periodic images of the nanoparticles. All the nanoparticles is fully relaxed before the BOMD simulation. An energy cutoff of 300 Ry is set for the plane wave basis set and VDW long range correction is added. The time step is 1 fs and the total simulation time for each system ranges from 20 ps, assuring that the system can reach the global optimal.

Supplementary Tables

Table S1: Surface energy, surface energy temperature coefficient, bond energy, atom size, excess surface enthalpy, and thermal expansion coefficient for the different mental elements.[14-17]

Category	mental	$\gamma(J/m^2)$	$-d\gamma/dT$	$H_s(J/m^2)$	$\alpha(K^{-1}\times10^{-6})$	$E_b(eV)$	r_0 (Å)
3-d serials	Fe	2.188	0.23	2.175	12.3	7.27	1.16
	Co	2.339	0.25	2.251	13.36	6.02	1.16
	Ni	2.538	0.28	2.415	13.3	4.92	1.15
	Cu	1.830	0.21	1.512	16.5	3.83	1.17

	Zn	1.197	0.18	1.200	25	1.89	1.25
4-d serials	Ru	3.075	0.34	3.079	9.1	8.21	1.25
	Rh	2.600	0.22	2.525	8.40	6.77	1.25
	Pd	1.690	0.17	1.662	11.2	5.19	1.28
	Ag	1.179	0.17	1.088	19.2	3.15	1.34
	Cd	0.819	0.13	0.803	29.8	1.27	1.41
5-d serials	Os	3.713	0.38	3.904	6.1	10.41	1.26
	Ir	3.028	0.31	3.009	6.8	8.17	1.27
	Pt	2.601	0.26	2.385	9	6.28	1.30
	Au	1.542	0.18	1.340	14.16	4.2	1.34

Table S2: The alpha-dependence of the surface energies for mentals (α=1.00, 1.12, and 1.49 corresponding to the sphere, icosahedron, and star-like shape, respectively.)

mental	α	$\gamma(J/m^2)$	mental	α	$\gamma(J/m^2)$	mental	α	$\gamma(J/m^2)$
Fe	1.00	2.228	Ru	1.00	3.829	Os	1.00	4.655
	1.12	2.443		1.12	4.320		1.12	5.151
	1.49	2.617		1.49	4.765		1.49	5.807
Co	1.00	3.031	Rh	1.00	2.524	Ir	1.00	2.796
	1.12	3.070		1.12	2.749		1.12	2.844
	1.49	3.095		1.49	2.906		1.49	2.908
Ni	1.00	2.023	Pd	1.00	1.829	Pt	1.00	2.185
	1.12	2.406		1.12	2.131		1.12	2.569
	1.49	2.462		1.49	2.357		1.49	2.892
Cu	1.00	1.893	Ag	1.00	1.169	Au	1.00	1.338
	1.12	2.077		1.12	1.212		1.12	1.571
	1.49	2.173		1.49	1.243		1.49	1.703
Zn	1.00	1.098	Cd	1.00	0.694			
	1.12	1.135		1.12	0.746			
	1.49	1.269		1.49	0.793			

Table S3: The bond energy (eV) of atomic species A and B (A and B represent the type of atoms in bimetallic system).

	Fe	Co	Ni	Cu	Zn	Ru	Rh	Pd	Ag	Cd	Os	Ir	Pt	Au
Fe	--	6.29	5.88	5.79	5.15	7.10	6.82	6.73	5.70	5.68	8.55	7.81	7.63	6.86
Co	--	--	5.24	5.15	4.52	6.46	6.18	6.09	5.07	5.04	7.91	7.18	7.00	6.23
Ni	--	--	--	4.74	4.10	6.05	5.77	5.68	4.65	4.63	7.50	6.76	6.58	5.81
Cu	--	--	--	--	4.02	5.96	5.68	5.59	4.56	4.54	7.41	6.67	6.50	5.73
Zn	--	--	--	--	--	5.32	5.05	4.96	3.93	3.91	6.78	6.04	5.86	5.09
Ru	--	--	--	--	--	--	6.99	6.90	5.87	5.85	8.72	7.98	7.80	7.03
Rh	--	--	--	--	--	--	--	6.62	5.59	5.57	8.44	7.70	7.53	6.76
Pd	--	--	--	--	--	--	--	--	5.50	5.48	8.35	7.61	7.43	6.67
Ag	--	--	--	--	--	--	--	--	--	4.45	7.32	6.59	6.41	5.64
Cd	--	--	--	--	--	--	--	--	--	--	5.88	5.51	5.42	5.04
Os	--	--	--	--	--	--	--	--	--	--	--	9.44	9.26	8.49
Ir	--	--	--	--	--	--	--	--	--	--	--	--	8.52	7.75
Pt	--	--	--	--	--	--	--	--	--	--	--	--	--	7.57
Au	--	--	--	--	--	--	--	--	--	--	--	--	--	--

Table S4: Parameters of the Gupta potential for the Ag-Ag, Cu-Cu, Au-Au, Pd-Pd, Ag-Cu, Au-Pd, Ag-Au, and Pd-Cu interactions.

	A (eV)	ξ (eV)	p	q	r_0 (Å)
Ag-Ag	0.1043	1.1940	10.79	3.190	2.890
Cu-Cu	0.0855	1.224	10.960	2.278	2.556
Au-Au	0.2061	1.790	10.229	4.036	2.884
Pd-Pd	0.1746	1.718	10.867	3.742	2.749
Ag-Cu	0.0944	1.2089	10.8746	2.734	2.723
Au-Pd	0.1896	1.7536	10.5431	3.889	2.816
Ag-Au	0.1490	1.4874	10.494	3.607	2.887
Pd-Cu	0.1221	1.4501	10.9135	3.01	2.6525

Table S5: The calculated Δh_i^{eff}, Δh_i^{size} and V_{ij} (in eV/atom) of Ag-Au bimetallic nanoparticles with the size (3 nm) and composition (A3B1) at different temperatures (400K, 600K, 800K).

Temperature	Δh_i^{eff}	Δh_i^{size}	V_{ij}
400	0.446	0.0292	-0.0315
600	0.613	0.0317	-0.0331
800	0.958	0.0363	-0.0359

Table S6: The comparison between the prediction results in this work and experiment results from literature.

Prediction in this work				
System	Chemical configuration	Heating temperature	Reshaping preference	Shape properties
Ag-Au	Core-shell	700K	Yes	star shape (core-shell)
Ag-Cu	Core-shell	750K	Yes	star shape (core-shell)
Au-Pd	Core-shell	870K	Yes	star shape (core-shell)
Au-Pt	Core-shell	910K	Yes	star shape (core-shell)
Pd-Cu	Core-shell	950K	No	Sphere (alloy)
Au-Cu	Core-shell	830K	No	Sphere (alloy)
Experiment results				

System	Chemical configuration	Heating method and temperature	Reshaping preference	Ref
Ag-Au	Core-shell	resistive heating (45℃)	Yes (star shape)	18
Ag-Cu	Core-shell	In situ STEM heating experiments (150℃)	Yes (star shape)	19
Au-Pd	Core-shell	calcination in static air (400℃)	Yes (star shape)	20
Au-Pt	Core-shell	hot solution pipette (160℃)	Yes (star shape)	21
Pd-Cu	Core-shell	Eurotherm programmable temperature controller (280℃)	No (Sphere-like alloy)	22
Au-Cu	Core-shell	temperature-dependent X-ray absorption fine (280℃)	No (Sphere-like alloy)	23

Supplementary Figures

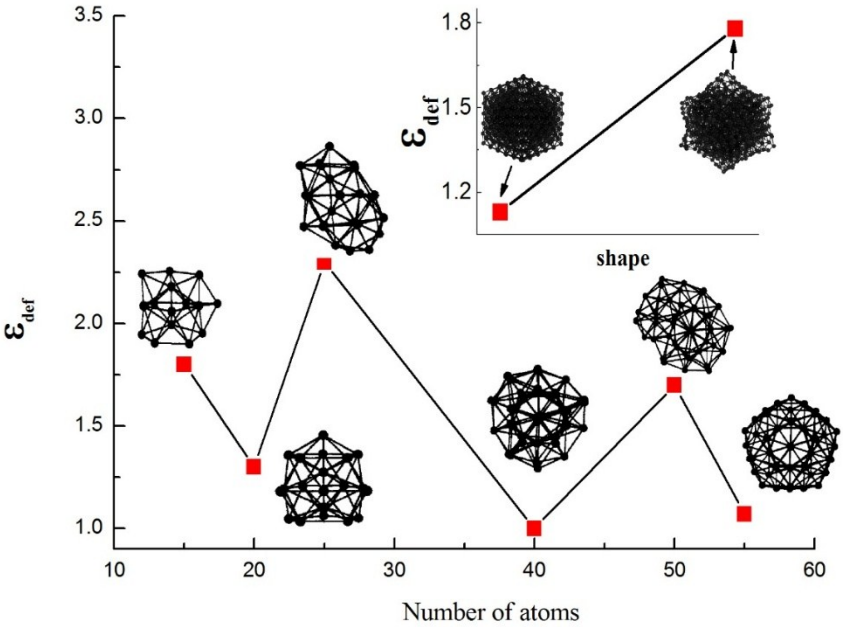

Fig. S1 The deformation parameter ε_{def} and responding snapshots of Ag clusters at different sizes.

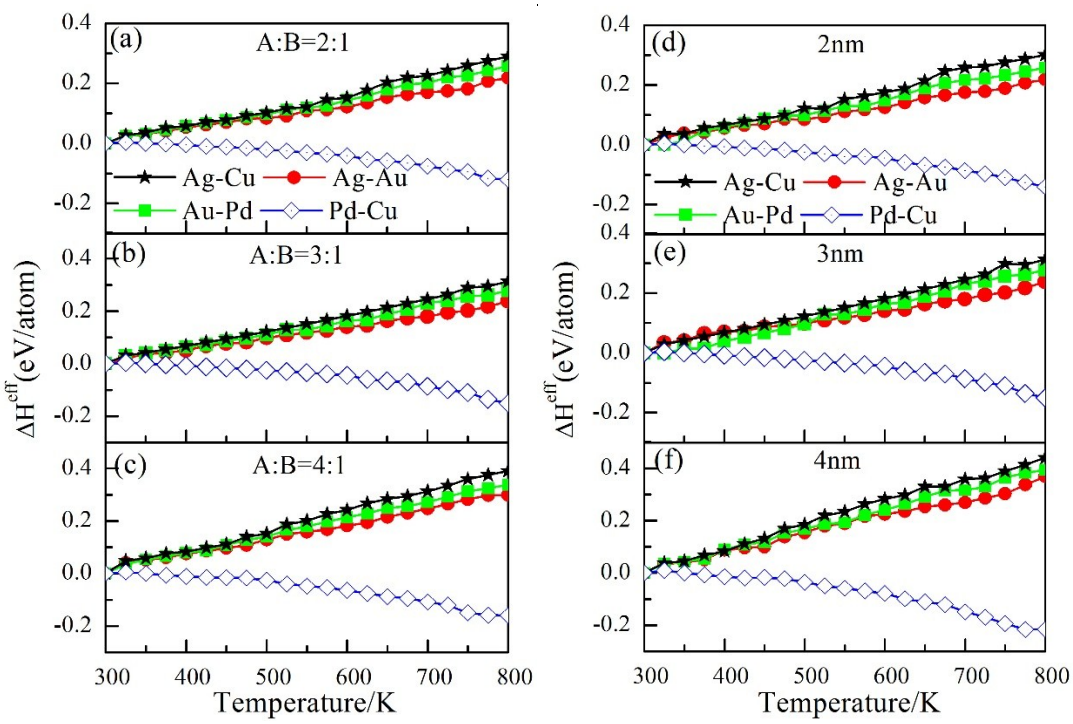

Fig. S2 The temperature dependent of ΔH^{eff} for Ag-Cu, Au-Pd, Ag-Au, and Pd-Cu bimetallic nanoparticles with the different compositions of A_2B_1 (a), A_3B_1 (b), and

A_4B_1 (c) (A represent Ag, Au, Ag, Pd, and B represent Cu, Pd, Au, Cu, respectively) and sizes of 2 nm (d), 3nm (e), and 4 nm (f) (fixed compositions: A_3B_1).

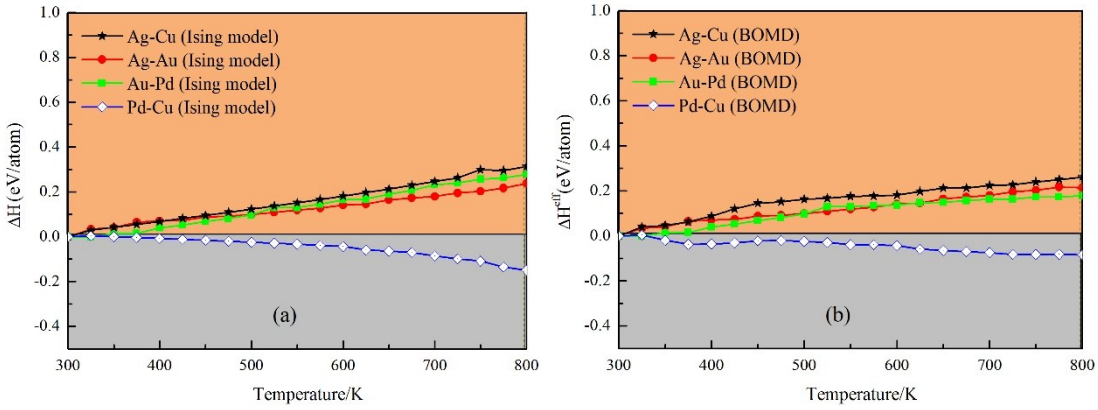

Fig. S3. The temperature dependent of ΔH for $Ag_{414}Cu_{147}$, $Au_{414}Pd_{147}$, $Ag_{414}Au_{147}$, and $Pd_{414}Cu_{147}$ core-shell bimetallic nanoparticles (3nm) with the different method including Ising method and BOMD.

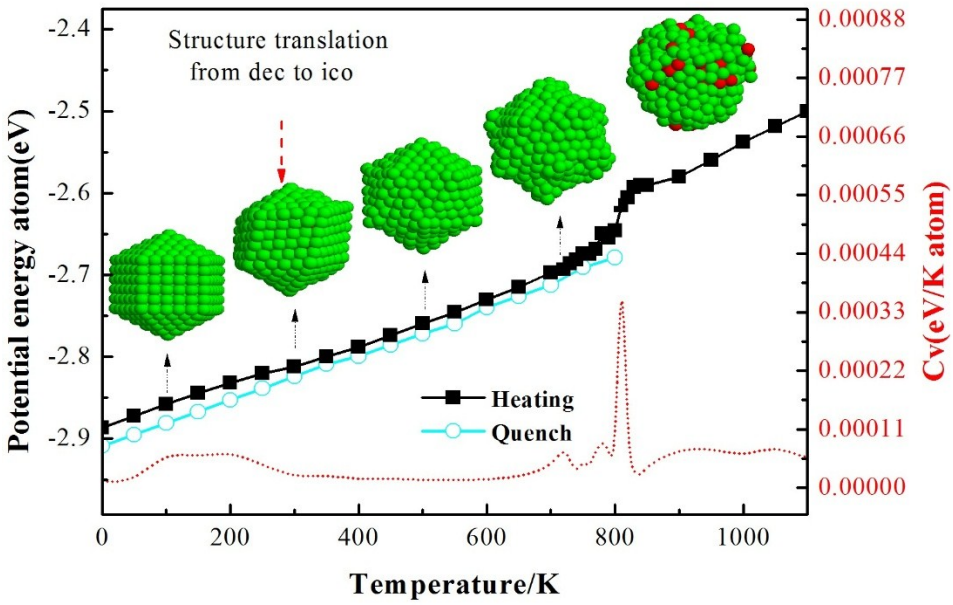

Fig. S4 The temperature dependent of caloric curves, the heat capacities Cv per atom, and corresponding snapshots (green: silver, red: copper) of decahedral (starting structure) $Ag_{414}Cu_{147}$ nanoparticles (3nm).

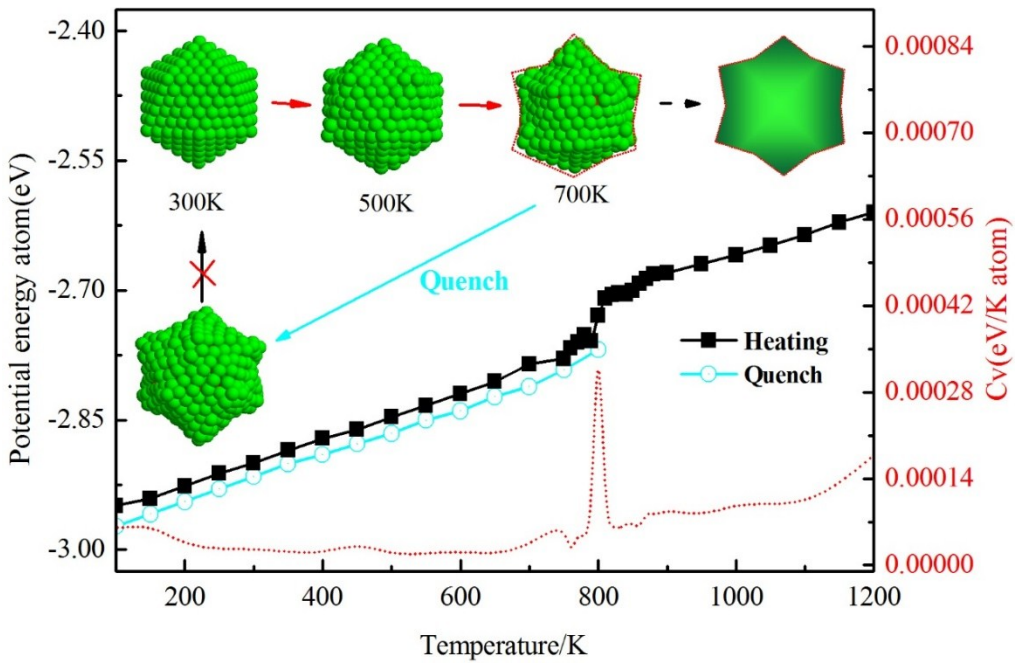

Fig. S5 The caloric curves, the heat capacities Cv per atom, and corresponding snapshots (green: silver, red: copper) of core-shell $Ag_{414}Cu_{147}$ nanoparticles (3nm) at different temperature.

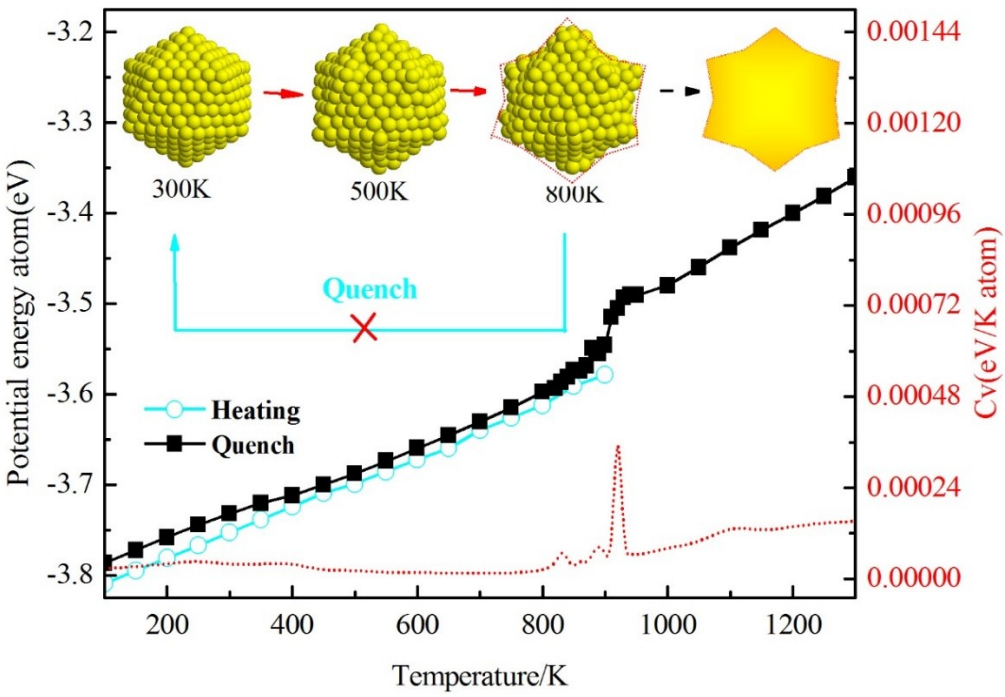

Fig. S6 The caloric curves, the heat capacities Cv per atom, and corresponding snapshots (yellow: gold, red: palladium) of core-shell $Au_{414}Pd_{147}$ nanoparticles (3nm) at different temperature.

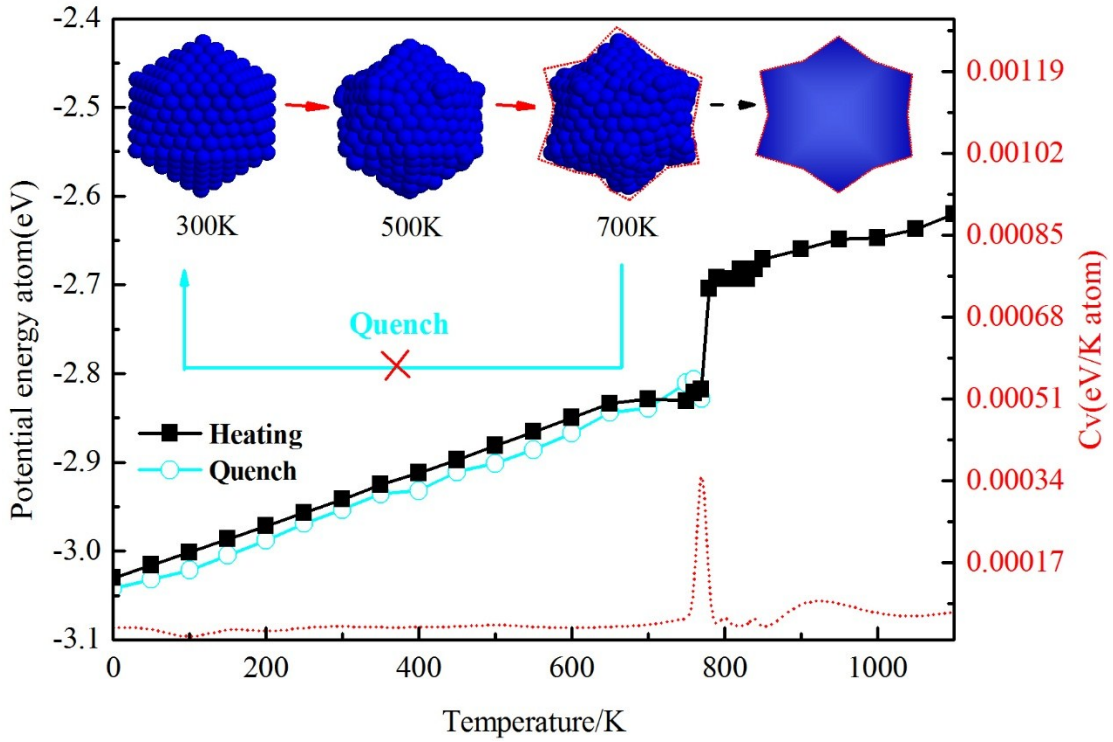

Fig. S7 The caloric curves, the heat capacities Cv per atom, and corresponding snapshots (blue: silver, red: gold) of core-shell $Ag_{414}Au_{147}$ nanoparticles (3nm) at different temperature.

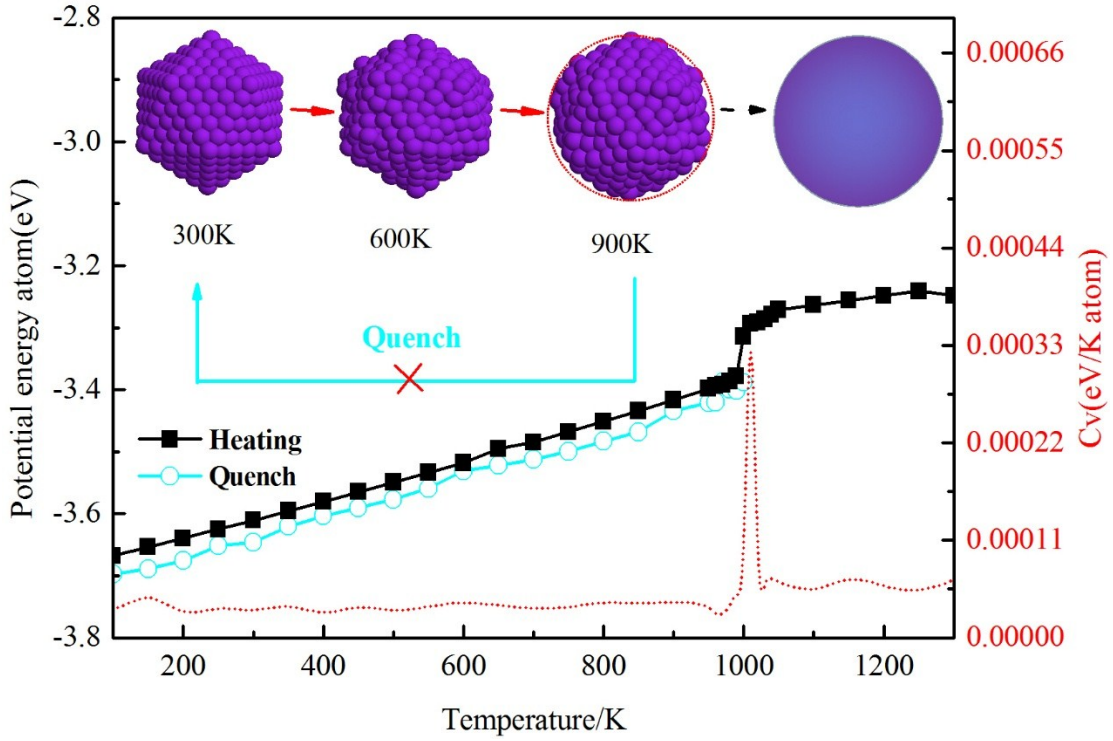

Fig. S8 The caloric curves, the heat capacities Cv per atom, and corresponding snapshots (purple: palladium, red: copper) of core-shell $Pd_{414}Cu_{147}$ nanoparticles (3nm) at different temperature.

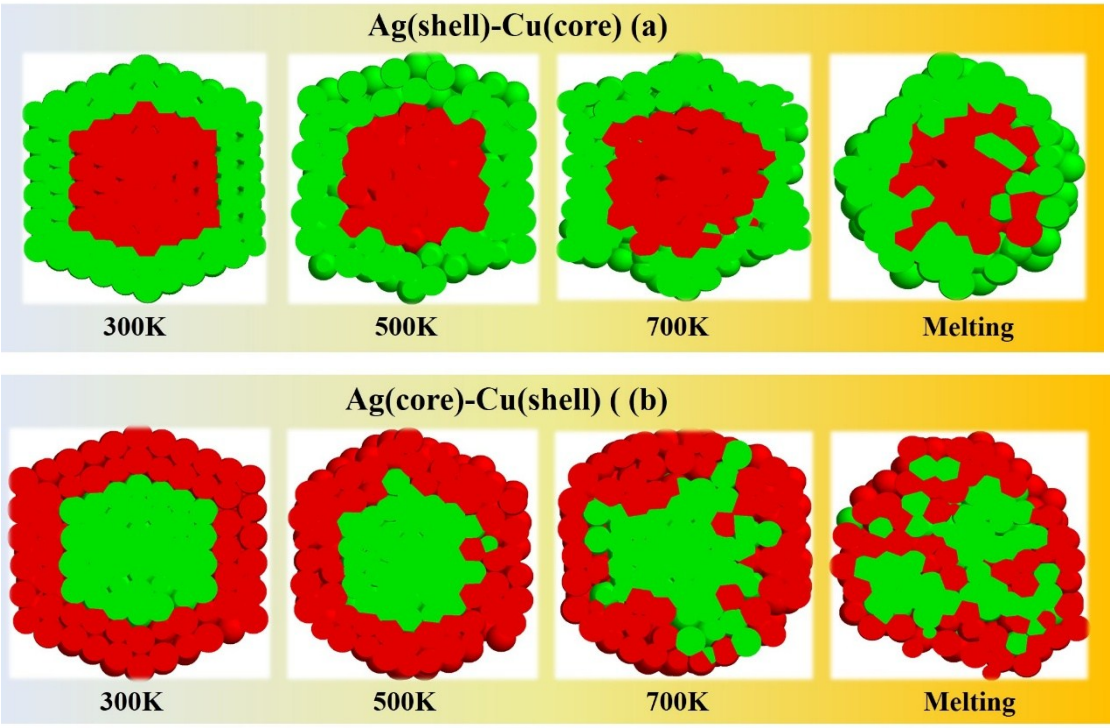

Fig. S9 The comparison of the structure evolution of $Ag_{shell}Cu_{core}$ and $Ag_{core}Cu_{shell}$ bimetallic nanoparticles in different temperatures (green: Ag atoms; red: Cu atoms).

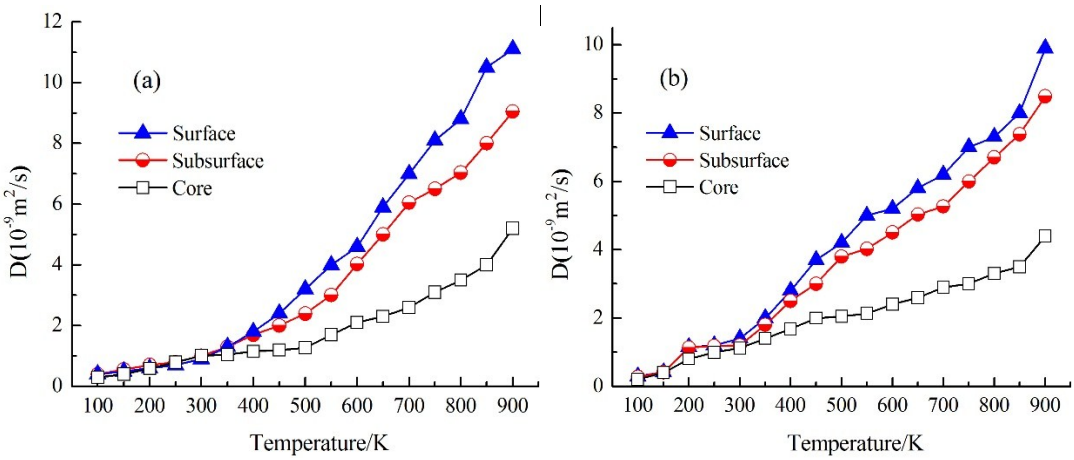

Fig. S10 The self-diffusivity coefficient, D of the (a) Au-Pd and Ag-Au bimetallic nanoparticles varying with different temperature.

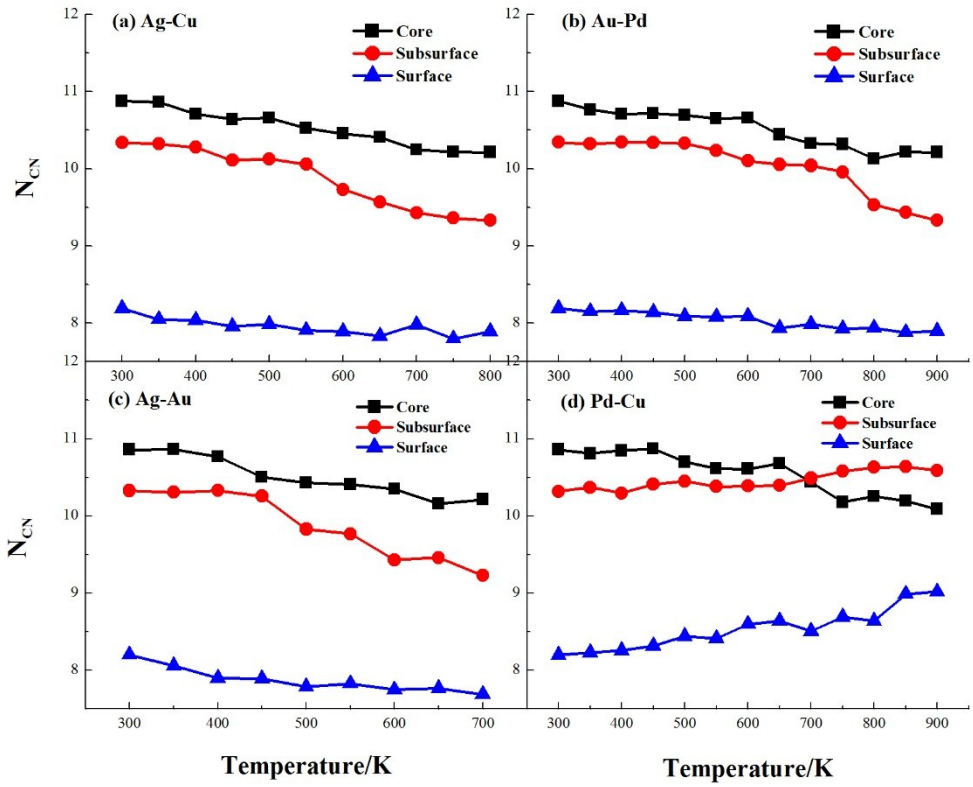

Fig. S11 The comparison of average coordination number (ACN) of surface, subsurface, and core atoms for $Ag_{414}Cu_{147}$ (a), $Au_{414}Pd_{147}$ (b), $Ag_{414}Au_{147}$ (c), and $Pd_{414}Cu_{147}$ (d) bimetallic nanoparticles, respectively.

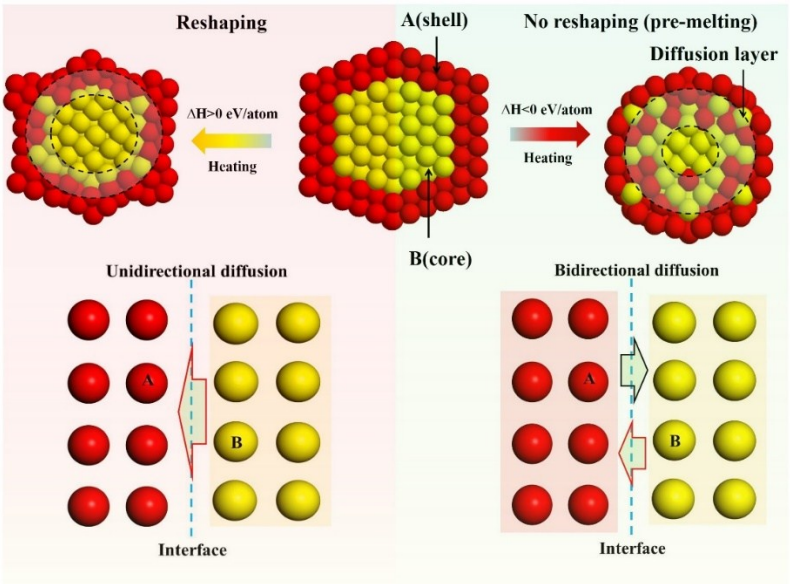

Fig. S12 Schematic of the diffusion process for bimetallic nanoparticles. Upon heating, the unidirectional diffusion (left) appears between A (shell) and B (core) and causes the reshaping of bimetallic nanoparticles. In contrast, the bidirectional diffusion (right) appear in bimetallic nanoparticles and cause the formation of spherical nanoparticles without reshaping.

Reference

1. Andriamiharintsoa, T. H.; Rakotomahevitra, A.; Piccolo, L.; Goyhenex, C., IrPd nanoalloys: simulations, from surface segregation to local electronic properties. *Journal of Nanoparticle Research* **2015,** *17* (5), 1-14.
2. Pastor, G. M.; Stampfli, P.; Bennemann, K. H., On the transition from Van der Waals- to metallic bonding in Hg-clusters as a function of cluster size. *Physica Scripta* **1988,** *38* (4), 623.
3. Tréglia, G.; Legrand, B.; Ducastelle, F., Segregation and ordering at surfaces of transition metal alloys: the tight-binding Ising model. *Europhys. Lett* **1988,** *7* (7), 575.
4. Moore, C. E., *Book Reviews: Atomic Energy Levels as Derived from the Analyses of Optical Spectra, 24Cr-41Nb*. U.S. National Bureau of Standards; for sale by the Supt. of Docs., U.S. Govt. Print. Off: 1953; p 391.
5. Cleri, F.; Rosato, V., Tight-binding potentials for transition metals and alloys. *Phys. Rev. B* **1993,** *48* (1), 22.
6. Cheng, D.; Huang, S.; Wang, W., Thermal behavior of core-shell and three-shell layered clusters: Melting of Cu_ {1} Au_ {54} and Cu_ {12} Au_ {43}. *Physical Review B* **2006,** *74* (6), -.
7. Kuntová, Z.; Rossi, G.; Ferrando, R., Melting of core-shell Ag-Ni and Ag-Co nanoclusters studied via molecular dynamics simulations. *Physical Review B* **2008,** *77* (20), 998-1002.
8. Rapallo, A.; Rossi, G.; Ferrando, R.; Fortunelli, A.; Curley, B. C.; Lloyd, L. D.; Tarbuck, G. M.; Johnston, R. L., Global optimization of bimetallic cluster structures. I. Size-mismatched Ag-Cu, Ag-Ni, and Au-Cu systems. *Journal of Chemical Physics* **2005,** *122* (19), 118-118.
9. Laasonen, K.; Panizon, E.; Bochicchio, D.; Ferrando, R., Competition between Icosahedral Motifs in AgCu, AgNi, and AgCo Nanoalloys: A Combined Atomistic–DFT Study. *Journal of Physical Chemistry C* **2013,** *117* (117), 26405-26413.
10. Zhao, Z.; Fisher, A.; Cheng, D., Phase diagram and segregation of Ag-Co nanoalloys: insights from theory and simulation. *Nanotechnology* **2016,** *27* (11), 492-498.
11. Rossi, G., .; Rapallo, A., .; Mottet, C., .; Fortunelli, A., .; Baletto, F., .; Ferrando, R., . Magic polyicosahedral core-shell clusters. *Physical Review Letters* **2004,** *93* (10), 105503.
12. eacute; Rives, B.; Catherinot, A.; Fr; eacute; eacute; Dumas-Bouchiat, R.; Champeaux, C.; Videcoq, A.; Ferrando, R., Growth of Co isolated clusters in the gas phase: Experiment and molecular dynamics simulations. *Physical Review B* **2008,** *77* (8), -.
13. Vandevondele, J.; Krack, M.; Mohamed, F.; Parrinello, M.; Chassaing, T.; Hutter, J., Quickstep : Fast and accurate density functional calculations using a mixed Gaussian and plane waves approach. *Computer Physics Communications* **2005,** *167* (2), 103-128.
14. Martienssen, W.; Warlimont, H., *Springer handbook of condensed matter and materials data =*. Springer: Berlin, 2005.
15. Borschevsky, A.; Pershina, V.; Eliav, E.; Kaldor, U., Relativistic coupled cluster study of diatomic compounds of Hg, Cn, and Fl. *Journal of Chemical Physics* **2014,** *141* (8), 084301.
16. Brooks, M. S. S.; Johansson, B., Exchange integral matrices and cohesive energies of transition metal atoms. *Journal of Physics F Metal Physics* **1983,** *13* (10), L197-L202.
17. Aqra, F.; Ayyad, A., Surface energies of metals in both liquid and solid states. *Applied Surface Science* **2011,** *257* (15), 6372–6379.
18. Cheng, L. C.; Huang, J. H.; Chen, H. M.; Lai, T. C.; Yang, K. Y.; Liu, R. S.; Hsiao, M.; Chen, C.

H.; Her, L. J.; Tsai, D. P., Seedless, silver-induced synthesis of star-shaped gold/silver bimetallic nanoparticles as high efficiency photothermal therapy reagent. *Journal of Materials Chemistry* **2012,** *22* (5), 2244-2253.

19. Lu, P.; Chandross, M.; Boyle, T. J.; Clark, B. G.; Vianco, P., Equilibrium Cu-Ag nanoalloy structure formation revealed by in situ scanning transmission electron microscopy heating experiments. *Apl Materials* **2014,** *2* (2), 1-980.

20. Herzing, A. A.; Carley, A. F.; Edwards, J. K.; Hutchings, G. J.; Kiely, C. J., Microstructural Development and Catalytic Performance of Au−Pd Nanoparticles on Al2O3 Supports: The Effect of Heat Treatment Temperature and Atmosphere. *Chemistry of Materials* **2008,** *20* (4), 1492-1501.

21. Bian, T.; Zhang, H.; Jiang, Y.; Jin, C.; Wu, J.; Yang, H.; Yang, D., Epitaxial Growth of Twinned Au-Pt Core-Shell Star-Shaped Decahedra as Highly Durable Electrocatalysts. *Nano Letters* **2015,** *15* (12), 7808-7815.

22. Mukundan, V.; Yin, J.; Joseph, P.; Luo, J.; Shan, S.; Zakharov, D. N.; Zhong, C. J.; Malis, O., Nanoalloying and phase transformations during thermal treatment of physical mixtures of Pd and Cu nanoparticles. *Science & Technology of Advanced Materials* **2014,** *15* (2), 025002.

23. Liu, S.; Sun, Z.; Liu, Q.; Wu, L.; Huang, Y.; Yao, T.; Zhang, J.; Hu, T.; Ge, M.; Hu, F., Unidirectional thermal diffusion in bimetallic Cu@Au nanoparticles. *Acs Nano* **2014,** *8* (2), 1886-1892.